

Nucleonic metamodelling in light of multimessenger, PREX-II and CREX data

C. Mondal^{1*} and F. Gulminelli^{2†}

¹*Laboratoire de Physique Corpusculaire, CNRS, ENSICAEN, UMR6534,
Université de Caen Normandie, F-14000, Caen Cedex, France*

(Dated: September 13, 2022)

The need of reconciling our understanding of the behavior of hadronic matter across a wide range of densities, especially at the time when data from multimessenger observations and novel experimental facilities are flooding in, has provided new challenges to the nuclear models. Particularly, the density dependence of the isovector channel of the nuclear energy functionals seems hard to pin down if experiments like PREX-II (or PREX) and CREX are required to be taken on the same footing. We put to test this anomaly in a semi-agnostic modelling technique, by performing a full Bayesian analysis of static properties of neutron stars, together with global properties of nuclei as binding energy, charge radii and neutron skin calculated at the semi-classical level. Our results show that the interplay between bulk and surface properties, and the importance of high order empirical parameters that effectively decouple the subsaturation and the supersaturation density regime, might partially explain the tension between the different measurements and observations. If the surface behaviors, however, are decoupled from the bulk properties, we found a rather harmonious situation among experimental and observational data.

I. INTRODUCTION

The electroweak probe of the isovector channel of the nuclear interaction obtained by studying the parity violating asymmetry in the elastic scattering channel, with the use of longitudinally polarized electrons as projectiles on neutron rich target nuclei *e.g.* ^{208}Pb (PREX, PREX-II) [1, 2] or ^{48}Ca (CREX), [3] has produced some very exciting discussions in recent times. Since the first run with ^{208}Pb nucleus in Jefferson lab [1], many theoretical studies were conducted using the data as a constraining probe for model building. Its lack of precision, however, failed to induce any significant improvement in the modeling of the isovector sector of the nuclear interaction. The second run, referred as PREX-II, was able to reduce the uncertainty in the measurement of amplitude of parity violation quite significantly. Its direct inference on the neutron skin (connected directly to the weak charge distribution inside nuclei) is however in a rift with inferences made by alternative hadronic probes [4–7]. Furthermore, explaining results on dipole polarizability, amplitudes of parity violation in both CREX and PREX-II within the density functional theory was found to be in a spot of bother, and the anomaly with respect to our previous understanding of the density dependence of symmetry energy became even more prominent [8–10]. It was pointed out [11–13] that the standard understanding of the neutron skin through density functional theory and its connection to the density dependence of the symmetry energy, particularly the slope parameter (L_{sym}), might miss some beyond mean-field contribution. However, the mean-field formalism has been extremely successful over the years in explaining a plethora of experimental data, and within this formalism a connection between the skin and the symmetry energy clearly exists [14–17]. In addition to nuclear structure observables, heavy ion collision experiments have provided

convincing constraints to the symmetry energy[18–20]. Even more stringent constraints come from neutron star observational data, pouring in during the past decade [21–31]. Those data opened up new frontiers in the nuclear theory providing a formidable boost to the understanding of dense nuclear matter, which is typically beyond our reach in the terrestrial experimental facilities.

This heavy supply of different types of data should help to pin down quite precisely the nuclear equation of state (EoS), and hopefully to connect it unequivocally to the underlying nuclear theory. Especially for this reason Bayesian studies have been employed quite frequently in recent times to extract the dense matter behavior in an agnostic way [32–46]. A certain degree of agnosticity is clearly required in order to extract the EoS from the astrophysical data in a model independent way. At the same time, the underlying correlations imparted on the theory by laboratory data at low densities coming from finite nuclei are also to be respected [47]. In the absence of a true theory that can explain the strong interaction from bottom up in the whole density regime covered by the experiments and the observations, functionals based on relativistic [48] or non-relativistic zero-range [49, 50] and finite-range [51] mean-field theory, and their multitude of extended versions are usually employed to build the nuclear EoS, see ref.[52], and references therein, for recent developments. These complex modelings often suffer from shortage in flexibility, though some efforts are being made presently to employ them in Bayesian studies for finite nuclear properties[53]. To address this limitation, a more general meta-modeling technique based on a density expansion in terms of empirical parameters of infinite nuclear matter was proposed [33]. This technique possesses the flexibility of agnostic approaches within the functional forms allowed by the hypothesis of beta-equilibrium in a matter composed of neutrons and protons. As such, it can also take care of the experimental constraints coming from laboratory by employing semi-classical approximations such as the extended Thomas-Fermi approach [54–56]. This approach also provides further advantage of treating the crust and core of neutron star matter

*Electronic address: mondal@lpccaen.in2p3.fr

†Electronic address: gulminelli@lpccaen.in2p3.fr

in unison [38, 57, 58], importance of which has been quantified in recent times [59, 60].

The present study is intended towards exploring in details the impact of recent measurement of neutron skin in ^{208}Pb and ^{48}Ca in Jefferson lab on the knowledge of the nuclear EoS, in light of the existing constraints from astrophysical observations. To this aim, we have employed the nuclear meta-model for the EoS, and put to use further an analytical version of the extended Thomas-Fermi (ETF) model to calculate few ground state properties of finite nuclei *e.g.* binding energy, charge radii, and neutron skin [54–56]. We performed a full Bayesian study for static astrophysical observables as well as ground state finite nuclear properties.

The paper is organized as follows. In Section II we outline briefly the meta-modeling of EoS and excerpts of the analytical ETF model developed by Aymard *et. al.* in Ref. [54, 55]. In section III we provide the details of the Bayesian analysis employed in this calculation. Our results are discussed in Section IV. The concluding remarks are drawn in Section V.

II. FORMALISM

A. EoS metamodel in β -equilibrium

The energy per particle of infinite homogeneous nuclear matter composed of neutrons and protons at density n_n and n_p , respectively, is written as[33],

$$e(n, \delta) = C_{kin} \sum_{q=n,p} \frac{n_q^{5/3}}{m_q^*(n, \delta)} + U_0(n) + U_{sym}(n)\delta^2, \quad (1)$$

where $n = n_n + n_p$ is the total density, $\delta = (n_n - n_p)/n$ is the isospin asymmetry, and $C_{kin} = 3(3\pi^2\hbar^3)^{2/3}/10$. The first term accounts for the zero point nuclear motion, and the dominant density dependence arising from the non-locality of the effective interaction, while the density dependence associated to the symmetric $U_0(n)$ and asymmetric $U_{sym}(n)$ part of the local nuclear potential is given by an agnostic Taylor expansion around the saturation point of symmetric matter n_{sat} as

$$U_{0,sym}(n) = \sum_{k=0}^4 \frac{(v_k)_{0,sym}}{k!} x^k u_k^{N=4}(x), \quad (2)$$

where $x = (n - n_{sat})/(3n_{sat})$, and $u_k^N(x) = 1 - (-3x)^{N+1-k} \exp(-b(1+3x))$ with b a correction ensuring the convergence at the zero-density limit. The density dependence of the effective masses m_q^* in Eq. (1) is governed by two parameters κ_{sat} and κ_{sym} [33] that are physically connected to the empirical value of the isoscalar effective mass m_{sat}^* and its isovector splitting $\Delta m^*/m$, both known experimentally, albeit with fair amount of uncertainties [61–67].

The coefficients $(v_k)_{0,sym}$ can be expressed solely in terms of the so-called nuclear matter empirical parameters (NMPs). These correspond to different coefficients of Taylor's expansion in density around the saturation point n_{sat} of the symmetric matter (SNM) energy $e_0(n) \equiv e(n, \delta)|_{\delta=0}$ and symmetry

energy $e_{sym}(n) \equiv \frac{1}{2} \frac{\partial^2 e}{\partial \delta^2} |_{\delta=0}$. Retaining up to fourth order, in $e_0(n)$ these are energy per particle E_{sat} , incompressibility K_{sat} , skewness Q_{sat} and stiffness Z_{sat} ; in $e_{sym}(n)$ they are symmetry energy E_{sym} , symmetry slope L_{sym} , symmetry incompressibility K_{sym} , symmetry skewness Q_{sym} and symmetry stiffness Z_{sym} . In both isoscalar and isovector sector, the NMPs are relatively tightly constrained by experiments up to order 2, thus allowing educated priors for the Bayesian treatment.

For the computation of the cold neutron star EoS, the composition of matter is determined by solving the coupled equations of nucleonic β -equilibrium,

$$\mu_n(n, \delta_\beta) - \mu_p(n, \delta_\beta) = \mu_e(n, \delta_\beta), \quad (3)$$

$$2 \left. \frac{\partial e(n, \delta)}{\partial \delta} \right|_n = \mu_e(n, \delta) - (m_n - m_p), \quad (4)$$

$$\mu_e = C_e \left[\gamma_r (1 + 6x_r^2) + \frac{x_r^2(2x_r^2 + 1)}{\gamma_r} - \frac{1}{\gamma_r} \right], \quad (5)$$

where $C_e = \frac{(m_e)^3}{8(3\pi^2 n_e)^{2/3}(\hbar c)^2}$, $x_r = \frac{\hbar c(3\pi^2 n_e)^{1/3}}{m_e}$, and $\gamma_r = \sqrt{1 + x_r^2}$; $\mu_{n,p,e}$ and $m_{n,p,e}$ are the chemical potentials and free masses of neutron, proton and electron, respectively; and n_e is the density of electrons. Muons appear in the system spontaneously when the lepton chemical potential μ_e exceeds the muon free mass m_μ , and their density is fixed by $n_\mu = n_p - n_e$ in the global equilibrium condition $\mu_\mu = \mu_e$. Once we get the composition solving the beta equilibrium equations, the baryonic pressure can be calculated as,

$$p_{bar}(n, \delta) = n^2 \frac{\partial e(n, \delta)}{\partial n}. \quad (6)$$

In the neutron star crust, the meta-modeling is extended to treat finite nuclei in the compressible liquid drop model (CLDM) approximation [68]. To describe a spherical nucleus of mass number A , charge Z , bulk density n_i and radius r_N in a spherical Wigner-Seitz (WS) cell of radius r_{WS} , the bulk energy $E_{bulk} = Ae(n_i, 1 - 2Z/A)$ is complemented with Coulomb, surface, and curvature terms. The Coulomb energy is given by:

$$E_{Coul} = \frac{8}{3} (\pi e Z n_i)^2 r_N^5 \eta_{Coul} \left(\frac{r_N}{r_{WS}} \right), \quad (7)$$

where e is the elementary charge, and the function $\eta_{Coul}(x)$ accounting for the electron screening is written as

$$\eta_{Coul}(x) = \frac{1}{5} \left[x^3 + 2 \left(1 - \frac{3}{2}x \right) \right]. \quad (8)$$

The surface and curvature energies are expressed as:

$$E_{surf} + E_{curv} = 4\pi r_N^2 \left(\sigma_s (Z/A) + \frac{2\sigma_c (Z/A)}{r_N} \right), \quad (9)$$

where σ_s and σ_c are the surface and curvature tensions, with an isospin dependence based on the behavior of Thomas-Fermi calculations at extreme isospin asymmetries [69]

$$\sigma_s(x) = \sigma_0 \frac{2^4 + b_s}{x^{-3} + b_s + (1-x)^{-3}}, \quad (10)$$

$$\sigma_c(x) = 5.5 \sigma_s(x) \frac{\sigma_{0,c}}{\sigma_0} (\beta - x). \quad (11)$$

For a set of bulk parameters appearing in the energy functional of Eq.(1), the bulk energy of any nucleus (A, Z) in the vacuum is given by $E_{bulk}^{vac} = Ae(n_i^{vac}, 1 - 2Z/A)$, where n_i^{vac} is the solution of the equation $\partial e(n, 1 - 2Z/A)/\partial n = 0$. The parameters corresponding to the surface and curvature terms $\sigma_0, \sigma_{0,c}, b_s$ and β are then optimized on the AME2016 mass table [57, 58, 70]. As a consequence, the physical correlation between bulk and surface parameters embedded in the empirical value of the nuclear masses is insured. The crustal EoS is finally determined by minimizing the energy of the WS cell with respect to the parameters defining the crustal composition $(A, Z, n_i, r_N, r_{WS}$, and the dripped neutron density n_q), as in refs. [57, 58, 68].

The CLDM description of the ground state of finite nuclei misses shell effects and specific properties of the effective nucleon-nucleon interaction such as spin-orbit coupling and tensor terms. Because of that, its predictive power is obviously quite limited. However, if the parameters are fitted on a large sample of nuclear masses it was recently shown that the CLDM energy compares reasonably well with more microscopic extended Thomas Fermi (ETF) approaches [71, 72]. Moreover, though the composition of the crust is not the same as the one obtained in full Hartree-Fock-Bogoliubov (HFB) theory, the crustal EoS is very well reproduced [73]. For this reason, we consider that the CLDM approach is sophisticated enough to realistically predict the NS crustal EoS. The improved treatment that we adopt to predict the ground state observables, notably the skin, is described in the next section.

B. Analytic Extended Thomas-Fermi method for nuclei

As far as ground state nuclear observables such as radii and skins are concerned, the CLDM approximation is not adequate and it is important to account for the full neutron and proton density profiles $n_n(r)$ and $n_p(r)$. Full HFB calculations including nuclear deformation and time-odd terms are in principle necessary for the purpose, and efficient numerical codes start to be available [74]. However, these approaches being numerically too expensive for a large Bayesian analysis, we resort to the ETF approximation, that was successfully compared with experimental data on binding energies and radii since many decades, see refs.[56, 75] for recent works, and references therein. Another advantage of the ETF method is that the integral expressions giving the nuclear energy and radii can be analytically calculated [54, 55] within some approximations that are well justified for nuclei not too far from stability as the ones considered in this section. This produces an analytical ETF mass formula that is ideally suited for the Bayesian analysis of the correlations between the observables and the EoS. The main aspects of the model are briefly recalled in this section, for more details see refs.[54, 55].

We start from the expression of the strong interaction part of the nuclear binding for a spherical nucleus in the ETF approximation:

$$E_{nuc} = 4\pi \int_0^\infty dr r^2 \mathcal{H}_{ETF}[n_n(r), n_p(r)]. \quad (12)$$

The ETF functional at the second order in \hbar is given by,

$$\begin{aligned} \mathcal{H}_{ETF}[n_n(r), n_p(r)] = & e(n_n, n_p)n_0 + \sum_{q=n,p} \frac{\hbar^2}{2m_q^*} \tau_{2q} \\ & + C_{fin}(\nabla n_0)^2. \end{aligned} \quad (13)$$

Here, $e(n_n, n_p)$ comes directly from the meta-model energy functional of Eq. (1), evaluated at the local densities. In Eq. (13), the local and non-local \hbar^2 corrections $\tau_{2q} = \tau_{2q}^l + \tau_{2q}^{nl}$ are given by,

$$\begin{aligned} \tau_{2q}^l &= \frac{1}{36} \frac{(\nabla n_q)^2}{n_q} + \frac{1}{3} \Delta n_q, \\ \tau_{2q}^{nl} &= \frac{1}{6} \frac{\nabla n_q \nabla f_q}{f_q} + \frac{1}{6} n_0 \frac{\Delta f_q}{f_q} - \frac{1}{12} n_q \left(\frac{\nabla f_q}{f_q} \right)^2, \end{aligned} \quad (14)$$

where $f_q = \frac{m}{m_q^*}$, with m the bare nucleon mass and m_q^* , $q = n, p$, giving the effective masses, already present in the zero order \hbar expression Eq. (1). C_{fin} is an extra parameter controlling the dominant gradient correction to the local functional. One may observe that realistic microscopic functionals contain more couplings related to gradient terms, notably at least the spin-orbit term. However, the associated parameters are strongly correlated. In order to pin down the EoS dependence, it was suggested that it might be sufficient to introduce a single effective C_{fin} parameter in the isoscalar sector [56]. We expect that the presence of extra couplings in finite nuclei with respect to the simplified case of homogeneous nuclear matter, will weaken the correlations between properties of finite nuclei and the nuclear EoS. Our choice of allowing for a unique gradient parameter will therefore give upper limits for those correlations. Anticipating our results, we will show that those correlations are weak, meaning that such upper limits are going to be quite significant. Concerning the isovector sector, an extra parameter Q is introduced below directly in the parametrization of the density profiles, to effectively account for isospin dependent gradient terms.

The densities in the ETF integral are commonly employed as Fermi functions to perform the integration analytically as,

$$\begin{aligned} n_q(r) &= n_{bulk,q} F_q(r), \\ F_q(r) &= \frac{1}{1 + e^{(r-R_q)/a_q}}, \\ n_{bulk,q} &= n_{bulk}(\delta) \frac{1 \pm \delta}{2}. \end{aligned} \quad (15)$$

Here, R_q and a_q are the radius and diffuseness parameters of the nucleon density profiles. The bulk density $n_{bulk}(\delta)$ and bulk asymmetry δ associated to a nucleus with proton number Z and neutron number N are determined by solving the following equations self-consistently [55],

$$\delta = \frac{\frac{N-Z}{A} + \frac{3a_c Z^2}{8QA^{5/3}}}{1 + \frac{9E_{sym}}{4QA^{1/3}}}, \quad (16)$$

$$n_{bulk}(\delta) = n_{sat} \left(1 - \frac{3L_{sym}\delta^2}{K_{sat} + K_{sym}\delta^2} \right), \quad (17)$$

$$a_c = \frac{3e^2}{20\pi\epsilon_0 r_{bulk}(\delta)}. \quad (18)$$

In the equations above, Q is the so-called surface stiffness, linked to the average distance between proton and neutron surfaces [76], and a_c is the Coulomb parameter with $r_{bulk} = (3/4\pi n_{bulk})^{1/3}$. With the approximation $a_n = a_p = a$, the diffuseness of the density distribution can be variationally obtained as [55],

$$a^2(A, \delta) = \frac{\mathcal{C}_{surf}^{NL}(\delta)}{\mathcal{C}_{surf}^L(\delta)} + \Delta R_{HS}(A, \delta) \sqrt{\frac{\pi}{\left(1 - \frac{K_{1/2}}{18J_{1/2}}\right)}} \times \frac{n_{sat}}{n_{bulk}(\delta)} \frac{3J_{1/2}}{\mathcal{C}_{surf}^L(\delta)} \sqrt{\frac{\mathcal{C}_{surf}^{NL0}}{\mathcal{C}_{surf}^{L0}}} (\delta - \delta^2). \quad (19)$$

In this equation, $J_{1/2}$ and $K_{1/2}$ are the symmetry energy coefficients of order 0 and 2, respectively, calculated at the density $n = n_{sat}/2$; $J_{1/2} = e_{sym}(n_{sat}/2)$, $K_{1/2} = 9(n_{sat}/2)^2 \partial^2 e_{sym} / \partial n^2 |_{n_{sat}/2}$. The coefficients $\mathcal{C}_{surf}^{L,NL}(\delta)$ and $\mathcal{C}_{surf}^{L0,NL0} \equiv \mathcal{C}_{surf,curv,ind}^{L,NL}(\delta = 0)$, depend both on the local interaction parameters $(v_k)_{0,sym}$ of Eq.(1) and on the effective masses, and their explicit expressions are given in Refs. [54, 55]. Finally, the hard sphere radii of the total (R_{HS}) and proton ($R_{HS,p}$) distribution are introduced as

$$\begin{aligned} \Delta R_{HS} &= R_{HS} - R_{HS,p} \\ &= r_{bulk}(\delta) A^{1/3} - r_{bulk,p}(\delta) Z^{1/3} \\ &= \left(\frac{3}{4\pi}\right)^{\frac{1}{3}} \left[\left(\frac{A}{n_{bulk}(\delta)}\right)^{\frac{1}{3}} - \left(\frac{Z}{n_{bulk,p}(\delta)}\right)^{\frac{1}{3}} \right]. \end{aligned} \quad (20)$$

The analytical expression for the diffuseness of the density profile in Eq. (19) allows one to compute the nuclear mass by direct integration of Eq. (12), with the addition of a Coulomb term,

$$M(A, Z) = Nm_n + Zm_p + E_{nuc}(A, Z) + a_c \frac{Z^2}{A^{1/3}}. \quad (21)$$

Moreover, once the mean square radii are given as

$$\langle r_q^2 \rangle = \frac{3}{5} R_{HS,q}^2 \left(1 + \frac{5\pi^2 a^2}{6R_{HS,q}^2} \right)^2, \quad (22)$$

the neutron skin Δr_{np} and the charge radii R_{ch} are obtained from,

$$\Delta r_{np} = \sqrt{\langle r_n^2 \rangle} - \sqrt{\langle r_p^2 \rangle}, \quad (23)$$

$$R_{ch} = \left[\langle r_p^2 \rangle + S_p^2 \right]^{\frac{1}{2}}. \quad (24)$$

The correction term S_p corresponds to the internal charge distribution of protons, which is taken as 0.8 fm [77, 78]. This quasi-analytic ETF method to calculate the gross properties of nuclei will be referred as “*aETF*” henceforth.

III. BAYESIAN ANALYSIS

We perform a Bayesian analysis for the different properties of nuclei using the *aETF* method described in the previous

section following Ref. [54, 55], as well as properties of neutron star following the metamodelling technique of Ref. [38]. First of all, the nuclear parameters that can be largely varied to build our prior EoS model, are the set of 12 NMPs corresponding to infinite nuclear matter, namely: n_{sat} , $E_{sat,sym}$, L_{sym} , $K_{sat,sym}$, $Q_{sat,sym}$, $Z_{sat,sym}$, $\kappa_{sat,sym}$. It was shown in Ref. [33] that, if the Taylor expansion is truncated at the order $N = 4$, to reproduce precisely any arbitrary nuclear model in a large density domain, it is necessary to consider different values for the third and fourth order NMPs *i.e.* $Q_{sat,sym}$ and $Z_{sat,sym}$ below and above n_{sat} , respectively. For this reason, we sample those NMPs as separate parameters below and above saturation density, leading to a total number of 16 independent NMPs. In this way, we make sure that the low density behavior of the EoS, as imposed by the observables sensitive to subsaturation density, does not impose any spurious correlation to the high density regime, where higher order derivatives start to play a role, and additionally different degrees of freedom may pop out [79]. We remark that this procedure does not include any discontinuity in the pressure nor in the sound speed. We denote henceforth the high order parameters above saturation with an asterisk mark ($Q_{sat,sym}^*$ and $Z_{sat,sym}^*$). The ranges for these NMPs used in the present work are provided in tabulated form in the supplemental material.

Apart from sampling the NMPs ruling the behavior of homogeneous nuclear matter with independent flat distributions, one needs further parameters C_{fin} and Q to calculate the properties of nuclei entering in Eqs. (12) and (13). We sample C_{fin} between 40 and 80 MeV in a flat distribution following the optimized value obtained in Ref. [56]. Concerning the surface stiffness Q , in principle this parameter can be extracted from semi-infinite nuclear matter slab calculations in the Thomas Fermi or ETF approximation [76]. This means that we expect it to be somehow correlated to the bulk parameters, to the gradient term C_{fin} and possibly to other gradient terms neglected in the present study. The importance of this correlation clearly depends on the detailed expressions assumed for the functional. For this reason, we have followed two different procedures corresponding to two extreme hypotheses on the degree of independence of Q from the rest of the parameter set. In the first, we sample Q fully agnostically within a flat probability distribution between 5 and 70 following the range of its values obtained in the literature [76, 80]. In a complementary method, we make use of the fact that Q was found to be linearly correlated with symmetry slope parameter L_{sym} across many popularly used mean field models in the literature. We sample Q according to its correlation with L_{sym} as depicted in Fig. 1. The Pearson correlation coefficient is -0.77 , which clearly points towards some ambiguity. To account for this deviation from the absolute correlation, we obtained the 99.9% confidence band of Q , from where we sampled Q randomly within its extremities for a given value of L_{sym} .

All in all, we performed our analysis with $N_p = 19$ parameters in Q - L_{sym} uncorrelated version, and with $N_p = 18$ parameters where further aid is taken from Fig. 1. The parameter set is collectively named as $\mathbf{X} \equiv \{X_k, k = 1, \dots, N_p\}$. The

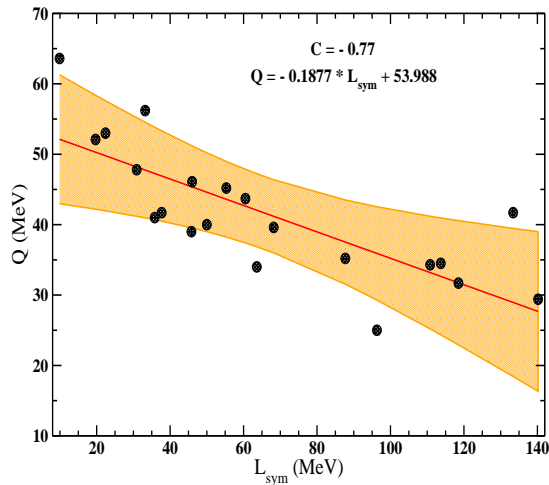


FIG. 1: (Color online) Surface stiffness Q plotted as a function of symmetry slope L_{sym} for the models given in Ref. [76] along with few more in Ref. [80]. The fitted straight line is also depicted in red accompanied by the Pearson correlation coefficient C .

prior distribution $P_{prior}(\mathbf{X}) = \prod_{k=1}^{N_p} P_k(X_k)$ of the *a-priori* uncorrelated parameter set is obtained with flat distributions $P_k(X_k)$, with intervals $\{X_k^{min}, X_k^{max}\}$ that are detailed in the supplemental material. The high density third and fourth order NMPS $Q_{sat,sym}^*$ and $Z_{sat,sym}^*$ were populated with the same limit as their non-asterisked partners. Posterior distributions are subsequently obtained using different physical filters, as outlined in the next section.

Filters

1. *AME+R_{ch}*: The standard likelihood expression for this filter is given by,

$$P_{AME+R_{ch}}(\mathbf{X}) \propto \omega_0 e^{-\chi_{AME}^2(\mathbf{X})/2} e^{-\chi_{R_{ch}}^2(\mathbf{X})/2} \prod_{i=1}^{N_p} P_i(X_i), \quad (25)$$

where $\omega_0 = 0$ or 1 depending on the meaningful production of nuclear masses and charge radii having a meaningful solution for the bulk asymmetry δ and the diffuseness of the density profile a ; and $P(\mathbf{X})$ corresponds to the flat prior distribution of different meta model and *aETF* parameters. The objective function for the AME2016 mass table and the experimental charge radii for a few spherical nuclei appearing above are defined by

$$\chi_{AME}^2(\mathbf{X}) = \frac{1}{N_1} \sum_n \frac{(M_{ETF}^{(n)}(\mathbf{X}) - M_{AME}^{(n)})^2}{\sigma_{BE}^2}, \text{ and}$$

$$\chi_{R_{ch}}^2(\mathbf{X}) = \frac{1}{N_2} \sum_n \frac{(R_{ch}^{ETF(n)}(\mathbf{X}) - R_{ch}^{exp(n)})^2}{\sigma_{ch}^2}. \quad (26)$$

Here, we have $N_1 = 2408$ and $N_2 = 9$. The σ_{BE} are chosen as 1% of the corresponding mass and $\sigma_{ch}^2 = 0.02$ fm for 7

nuclei and 0.1 for 2 nuclei. The specifics of the charge radii [81] used in the present work are detailed in the supplemental material.

Since a satisfactory reproduction of mass and radii is a necessary condition for using a nuclear functional in the reproduction of more sophisticated observables such as the nuclear skin, the successive filters are all applied on top of *AME+R_{ch}*, such that this first posterior plays the role of a prior informed by nuclear experiments on ground state properties. The posterior probability distributions of the set \mathbf{X} of EoS and *aETF* parameters for other filters are conditioned by likelihood models of the different observations and constraints \mathbf{c} with normalizing constant \mathcal{N} as:

$$P(\mathbf{X}|\mathbf{c}) = \mathcal{N} P_{AME+R_{ch}}(\mathbf{X}) \prod_k P(c_k|\mathbf{X}). \quad (27)$$

The corresponding probability distributions for the observables $Y(\mathbf{X})$ are obtained by an overall marginalization through the range of values of parameters \mathbf{X} between \mathbf{X}_{min} and \mathbf{X}_{max} according to

$$P(Y|\mathbf{c}) = \prod_{k=1}^N \int_{X_k^{min}}^{X_k^{max}} dX_k P(\mathbf{X}|\mathbf{c}) \delta(Y - Y(\mathbf{X})). \quad (28)$$

2. *χ -EFT*: The next filter we apply on our nuclear physics informed prior is the constraints on symmetric nuclear matter (SNM) and pure neutron matter (PNM) at low densities from 0.02 - 0.2 fm⁻³ obtained by theoretical calculations from the chiral effective field theory (*χ -EFT*) [82]. The probability of the posterior distribution can be outlined as

$$P_{\chi-EFT}(\mathbf{X}) \propto \omega_{\chi-EFT}(\mathbf{X}) P_{AME+R_{ch}}(\mathbf{X}), \quad (29)$$

where, $\omega_{\chi-EFT} = 0$ or 1, depending on whether they pass through the area predicted by the *χ -EFT* calculations. This theoretical band is interpreted as a $1 - \sigma$ uncertainty, and for this reason a 5% extension is added on the edges.

3. *Astro*: The high density part of the nuclear matter is known to be quite sensitive to the constraint on the observed maximum mass of neutron star obtained by measuring Shapiro delay [21, 22]. We outlined the likelihood probability of a model \mathbf{X} by taking a cumulative Gaussian distribution function for the observed maximum mass M_{max} as depicted in Ref. [22] with mean at $2.01M_\odot$ with variance $0.04M_\odot$ as,

$$P(M_{max}|\mathbf{X}) = \frac{1}{0.04\sqrt{2\pi}} \int_0^{M_{max}(\mathbf{X})/M_\odot} e^{-\frac{(x-2.01)^2}{2 \times 0.04^2}} dx. \quad (30)$$

Some effects are also imparted by the data on joint tidal deformability $\tilde{\Lambda}$ of the GW170817 event, which is defined as

$$\tilde{\Lambda} = \frac{16}{13} \frac{(m_1 + 12m_2)m_1^4\Lambda_1 + (m_2 + 12m_1)m_2^4\Lambda_2}{(m_1 + m_2)^5}, \quad (31)$$

where, m_1, m_2 are the masses of the merging NS system and Λ_1, Λ_2 are their respective tidal deformabilities, which are connected to the mass M and radius R of the corresponding system as $\Lambda \propto (R/M)^5$. The GW170817 event gives direct

constraint on the $\tilde{\Lambda}$ and mass-ratio q for an event with chirp mass $\mathcal{M}_{chirp} = 1.186 \pm 0.001 M_{\odot}$ in a three dimensional posterior probability distribution. As \mathcal{M}_{chirp} is very precisely measured, we defined the likelihood as

$$P(LVC|\mathbf{X}) = \sum_i P_{LVC}(\tilde{\Lambda}(q^{(i)}), q^{(i)}), \quad (32)$$

where, $P_{LVC}(\tilde{\Lambda}(q), q)$ is the approximated two dimensional posterior probability from GW170817 event obtained by LIGO-Virgo collaboration (LVC) [29], which we interpolated for each \mathbf{X} in our calculation by sampling $q \in [0.73, 1.00]$ and calculating the corresponding masses, making the approximation $\mathcal{M}_{chirp} = 1.186$ for all samples, as

$$\mathcal{M}_{chirp} = \frac{(m_1 m_2)^{3/5}}{(m_1 + m_2)^{1/5}} = \frac{q^{3/5} m_1}{(1+q)^{1/5}}, \quad (33)$$

and the corresponding $\tilde{\Lambda}$ from Eq. (31).

Finally, the posterior probability of this distribution is written as:

$$P_{astro}(\mathbf{X}) \propto \omega_{astro} P(M_{max}|\mathbf{X}) P(LVC|\mathbf{X}) P_{AME+R_{ch}}(\mathbf{X}). \quad (34)$$

Here, ω_{astro} is a pass-band type filter similar to $\omega_{\chi-EFT}$ in Eq. (29). This filter eliminates models which violate causality or thermodynamic stability, or exhibit negative symmetry energy at densities lower than the central density of the highest NS mass M_{max} for the corresponding sample, or leading to a non-convergent solution for the variational equations of the crust. We do not explicitly include the information from NICER observations [23–26], because it was shown in ref.[38] that the present uncertainties are such that these observations do not add major constraints on the metamodeling parameters, if the model is already informed by the GW170817 gravitational wave data.

4. *PREX-II+CREX*: The posterior probability of this distribution is written as:

$$P_{PREX+CREX}(\mathbf{X}) \propto e^{-\chi_{skin}^2(\mathbf{X})/2} P_{AME+R_{ch}}(\mathbf{X}), \quad (35)$$

where the cost function for the neutron skin measurement is defined by

$$\chi_{PREX+CREX}^2(\mathbf{X}) = \frac{(\Delta r_{np}^{208}(\mathbf{X}) - \Delta r_{np}^{PREX-II})^2}{(0.07)^2} + \frac{(\Delta r_{np}^{48}(\mathbf{X}) - \Delta r_{np}^{CREX})^2}{(0.05)^2}. \quad (36)$$

Here, $\Delta r_{np}^{208}(\mathbf{X})$ and $\Delta r_{np}^{48}(\mathbf{X})$ are the values of Δr_{np} in fm corresponding to ^{208}Pb and ^{48}Ca nuclei, calculated with the parameter set \mathbf{X} . The values of $\Delta r_{np}^{PREX-II} = 0.283$ fm $\Delta r_{np}^{CREX} = 0.121$ are taken from Refs. [2, 3], respectively. It is important to point out here that, we have applied these filters from PREX-II and CREX separately as well, to observe their individual impact on different observables of interest.

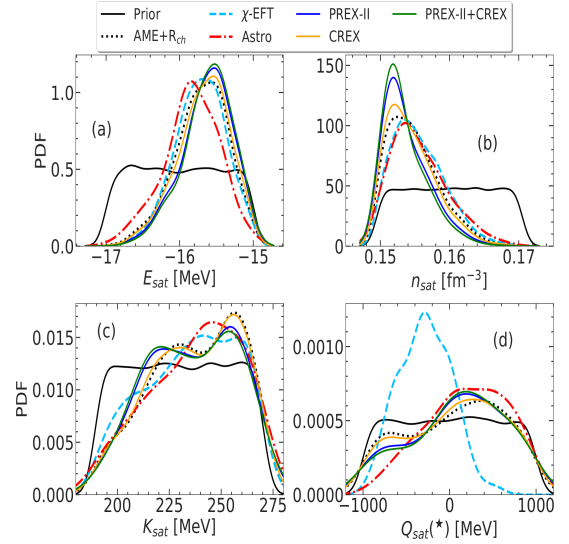


FIG. 2: (Color online) Posterior probability distributions of different empirical parameters corresponding to the symmetric nuclear matter obtained with different filters described in Section III.

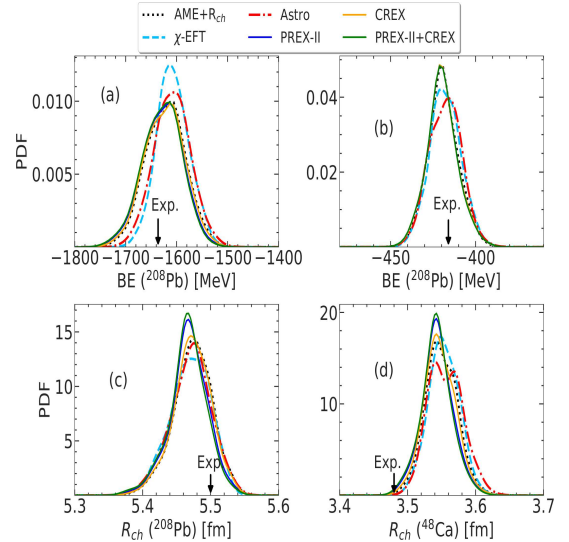


FIG. 3: (Color online) Posterior probability distributions of binding energies (upper panels) and charge radii (lower panels) of ^{208}Pb (left) and ^{48}Ca (right) nuclei obtained with the *aETF* method corresponding to the same filters as in Fig. 2.

IV. RESULTS

In Fig. 2 we plot the one dimensional probability distributions of different empirical parameters corresponding to symmetric matter using the filters described in Sec. III, and the sampling of Q parameter following the correlation systematics of Fig. 1. The behavior is almost indistinguishable from the one obtained with the other method of Q sampling. The latter is thus only presented in the supplemental material. The separate effects of PREX-II and CREX are also displayed in the figure. Since *AME+R_{ch}* is informed by nuclear data,

one can already observe peaks in the distributions for E_{sat} and n_{sat} around -16.1 MeV and 0.154 fm $^{-3}$, respectively, and the distributions of those parameters get only marginally affected by the subsequent information from nuclear theory, skin data, or astrophysical observations. The effect of the mass constraint gets diluted in K_{sat} and degrades further in Q_{sat} . We do not include results for the fourth-order parameters Z_{sat} , Z_{sat}^* because they have very large uncertainties and very little impact from the different constraints. The same applies to Z_{sym} , Z_{sym}^* in the symmetry energy sector, to be shown in the upcoming figures. The peak in n_{sat} at the level of mass-informed prior was not observed in a study performed with a similar technique in Ref. [38]. Anticipating the results from the correlation study below, this occurs here because of the inclusion of the constraints on charge radii using the *aETF* method in the present calculation, while only binding energy constraints were used in Ref. [38]. One can also observe that the data on neutron skins from CREX and PREX-II have no impact on these isoscalar properties, which is expected.

In Fig. 2(d), the quantity represented is the skewness Q_{sat} below saturation for all distributions except *Astro*. For that, we have plotted the effective supersaturation skewness parameter Q_{sat}^* , which is constrained better by this filter, particularly being sensitive to the high density behavior of the EoS. The distinct peak appearing for Q_{sat} in χ -EFT, which is located at a different place than that in *Astro*, does not therefore point towards a possible tension between nuclear theory and astrophysical measurements. It rather emphasizes the fact that the high density EoS behavior cannot be extrapolated from the sub-saturation EoS, even in the conservative hypothesis that no exotic degrees of freedom appear at high density. Indeed, higher order terms in the Taylor expansion become dominant at high density, and are here effectively summed up as a Q_{sat}^* contribution. We will further comment this point in the correlation study below.

In Fig. 3 we plot the distribution of binding energies and charge radii for ^{208}Pb and ^{48}Ca for different filters using the *aETF* method corresponding to the Q sampling of Fig. 1. The situation is almost identical with the independent sampling of Q (not shown). We depict only the cases of ^{208}Pb and ^{48}Ca for illustrative purpose and mainly because data from PREX-II and CREX correspond to those specific nuclei. The corresponding experimental values are indicated by arrows for all four observables. Similar behaviors were observed for other nuclei in our nuclear physics informed prior *AME+R_{ch}*. They are explicitly shown in the supplemental material. The reproduction of ground state radii are not fully satisfactory, but this limitation is shared by more microscopic mean field studies [83, 84]. It is known that a precise reproduction of specific charge radii at the mean field level requires fine tuning of the interaction [85], which points towards an important effect of beyond mean-field correlations or higher order terms in the functional, not linked to EoS properties [86]. The different filters play almost no role in the distribution the binding energies of ^{208}Pb and ^{48}Ca (see also supplemental material). This is consistent with the observation of Fig. 2(a) and 2(b).

Quite distinct behaviors are observed for the symmetry energy parameters *e.g.* E_{sym} , L_{sym} , K_{sym} , Q_{sym} and Q_{sym}^* for

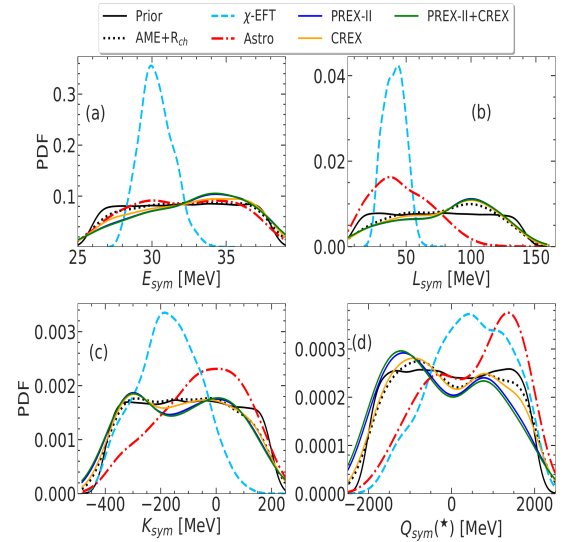


FIG. 4: (Color online) Posterior probability distributions of different empirical parameters corresponding to the density behavior of the symmetry energy obtained with different filters described in Section III. The surface stiffness Q is sampled independently from the bulk parameters in the prior.

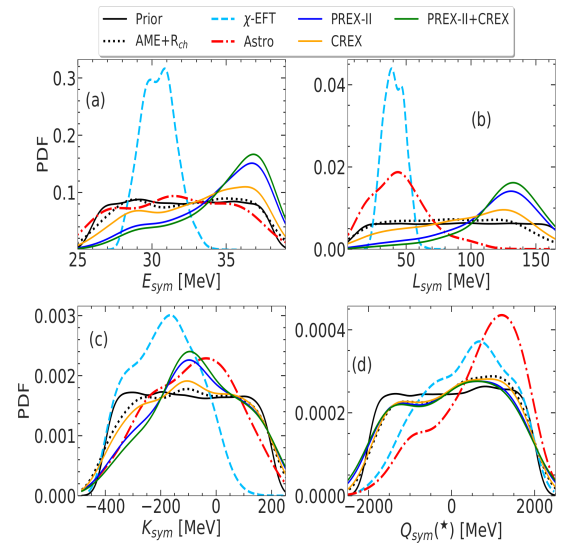


FIG. 5: (Color online) Posterior probability distributions of different empirical parameters corresponding to the the density behavior of the symmetry energy, obtained with different filters described in Section III. The surface stiffness Q prior is obtained following the correlation of Fig. 1.

both the sampling methods of Q , as shown in Figs. 4 and 5. As already reported in previous studies [38], the χ -EFT calculations offer a fairly precise knowledge on the low order empirical parameters in the symmetry energy sector, while this constraint gets relaxed as higher order parameters are put to test. Since the χ -EFT filter only concerns bulk matter properties, the corresponding posteriors are independent of the distribution of the surface stiffness parameter Q . The impact of astrophysical measurement through the *Astro* constraints

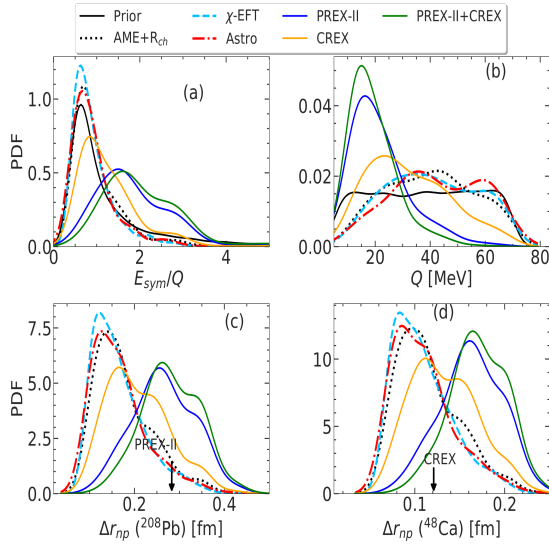


FIG. 6: (Color online) Posterior probability distribution of E_{sym}/Q , L_{sym} and Δr_{np} of ^{208}Pb and ^{48}Ca nuclei obtained with different filters using the models where the surface stiffness Q is sampled independently from the bulk parameters in the prior.

is also consistent with the one reported in the literature [38]. Models in the prior with very high values of L_{sym} get ruled out because of non-existence of meaningful solution of the AME2016 mass table, and the effect is particularly important in the correlated sampling technique, where L_{sym} directly impacts the surface properties. In the uncorrelated sample, we observe that the constraint from the skin measurements does not affect the values of the bulk parameters. Conversely, all symmetry parameters up to order 2 are found to be peaked at higher values for the *PREX-II* and *PREX-II+CREX* posteriors in the correlated sampling compared to the uncorrelated one, and to the corresponding nuclear physics informed *AME+R_{ch}* posteriors. It is also interesting to note that *Astro* posteriors show distinct peaks in L_{sym} , K_{sym} and Q_{sym}^* , following rather closely the concerned χ -*EFT* posteriors in Figs. 4 and 5.

To understand these distinct behaviors, we show the neutron skin and Q distributions in Fig. 6 for agnostic sampling of Q , and in Fig. 7 for the sampling of Q following Fig. 1. We can see the effect of the dependence of Q on L_{sym} in the correlated sampling technique; very small values of Q getting suppressed in the *Prior* and *AME+R_{ch}* posterior of Fig.7. A particular parameter of interest to look into is the ratio between symmetry energy E_{sym} and stiffness parameter Q . It was shown in semi-infinite matter calculations across many relativistic and non-relativistic interactions [76], that E_{sym}/Q is linearly correlated with Δr_{np} almost in a model independent way. In panel (a) of Fig. 6 and 7, the posterior probability distribution for this ratio is depicted for different filters. The findings of Ref.[76] are nicely confirmed by our study: the distribution of Δr_{np} for ^{208}Pb [cf. Fig 6(c) and 7(c)] and ^{48}Ca [cf. Fig 6(d) and 7(d)] follow very sharply the corresponding distribution of E_{sym}/Q , respectively.

As in the correlated sampling, small values of Q (and there-

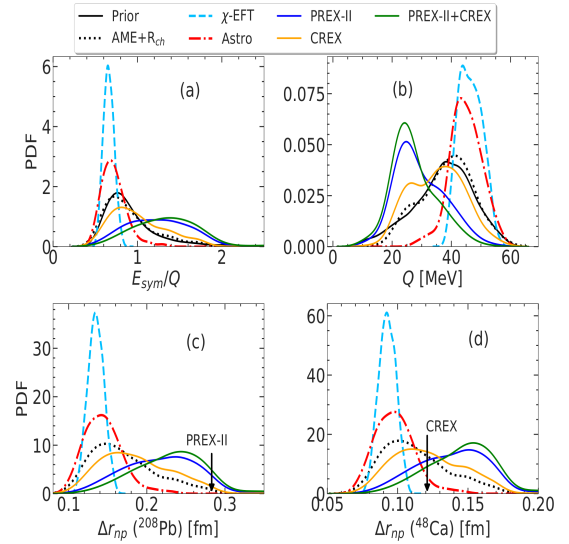


FIG. 7: (Color online) Same as Fig. 6, but with models where Q and L_{sym} are connected by Fig. 1.

fore, high values of E_{sym}/Q and large skins as measured by *PREX-II* are available only for large values of L_{sym} , the *PREX-II* filter produces a stark contrast in the distribution of L_{sym} in Fig. 4(b) and 5(b). Specifically, the agnostic sampling of Q makes L_{sym} free from skin in Fig. 4(b), whereas, L_{sym} observes an apex in Fig. 5(b) at rather larger values ~ 120 MeV with the *PREX-II* filter. This value is not far from the value of $L_{sym} = 106 \pm 37$ MeV, inferred by the authors of Ref.[87] from the *PREX* data. It is important to recognize here that, density functionals were employed to infer the L_{sym} values in Ref. [87], and we can therefore expect that a correlation similar to the one of Fig. 1 was present in that study.

In the case of the uncorrelated sample in Fig. 6, the *PREX-II* and *CREX* posteriors of Δr_{np} are clearly peaked on the corresponding experimental values as expected. However, if both *PREX-II* and *CREX* results are simultaneously taken into account, the prediction for the skin of ^{48}Ca gets displaced from the experimental value (see Fig. 6(d)). This suggests some unintelligible elements in the ^{208}Pb data, as indicated in the latest paper of the collaboration [3]. The possible anomaly of the ^{208}Pb data is further suggested by the results obtained with the correlated sample in Fig.7(c). Here we can see that imposing the *PREX-II* filter does not result in reproducing the *PREX-II* data satisfactorily, in particular, it fails to reach the higher end of the $1\text{-}\sigma$ limit. This means that the E_{sym}/Q distribution is peaked on too low values to reproduce the skin measurement. This can be understood from the fact that the constraint imposed by the nuclear masses and radii reduce the probability of keeping very large values of L_{sym} in the correlated sampling, as described in Fig. 5(b) explicitly. This in turn limits retaining very small values of Q (see Fig. 7(b)) and hence large E_{sym}/Q and Δr_{np} . This result is in qualitative agreement with the recent findings of ref. [9], where a difficulty was reported in simultaneously reproducing the ^{208}Pb and ^{48}Ca data with energy functionals that give a satisfactory

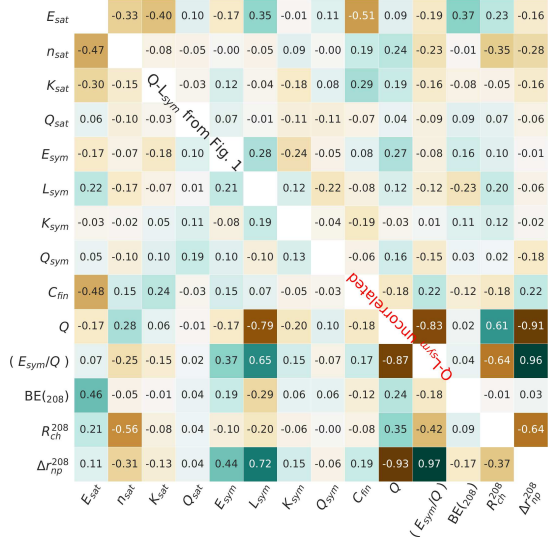


FIG. 8: (Color online) Pearson correlation matrix between various parameters of the metamodel as well as observables of interest obtained with the $AME+R_{ch}+PREX-II+CREX$ (see text for more details) filter. The numbers below the diagonal correspond to the case where Q and L_{sym} are sampled from Fig. 1; the numbers above the diagonal correspond to the independent sampling of Q and L_{sym} .

description of masses and charge radii throughout the nuclear chart.

This effect is even more pronounced if we consider the χ -EFT filter. The theoretical χ -EFT results strongly constrain L_{sym} towards low values, and therefore the corresponding posterior is not compatible with the PREX-II data, if a strong correlation is assumed between E_{sym}/Q and L_{sym} (see Fig.7(c),(d)). On the contrary, no strong tension is observed if the surface symmetry properties are independently sampled (see Fig. 6(c),(d)). The CREX posteriors, on the other hand, have large overlap with the χ -EFT posteriors.

Finally, in Fig 6 we can observe that the astrophysical observations (lines noted *Astro*) have negligible impact on the skin prediction following closely the $AME+R_{ch}$ lines, as expected, though it shows some impact on low order EoS parameters like L_{sym} and K_{sym} (see Figs. 4- 5). One can observe, however, a strong tension between *Astro* (informed by GW170817 LIGO-Virgo observation) and $PREX-II$ posteriors in Fig. 7. This is primarily manifested through the restriction of smaller Q (Fig. 7(b)) via its *a-priori* assumed correlation with L_{sym} through Fig. 1.

The distributions displayed in the previous figures can be interpreted further by looking at the correlations among the different observables and parameters. In Fig. 8 we show the Pearson correlation coefficients between different quantities of interest obtained for the $AME+R_{ch}$ plus $PREX-II+CREX$ filter, with agnostic sampling of the Q above the diagonal, and with correlated sampling of the same below the diagonal. Masses and radii are only correlated to E_{sat} and n_{sat} , respectively, the latter correlation being highly enhanced in the correlated sampling. Absolute correlation between E_{sym}/Q and Δr_{np} is also noticeable irrespective of the filters and sam-

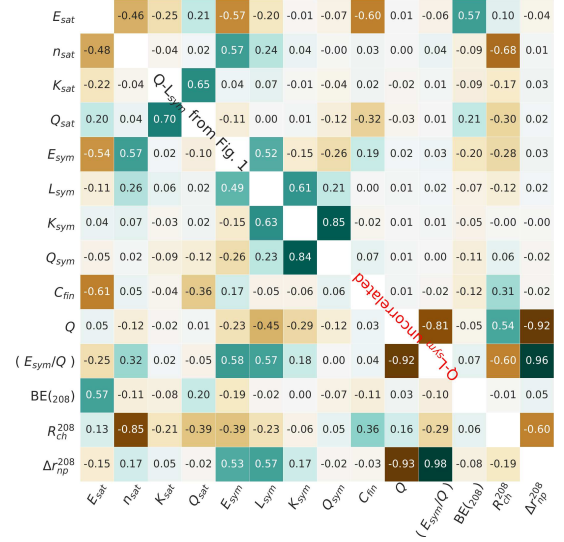


FIG. 9: (Color online) Same as Fig. 8, but obtained with χ -EFT filter.

pling techniques [76]. The absence of any other correlations, except a loose correlation between E_{sat} and K_{sat} , is due to the importance of gradient terms that are here treated independently from bulk terms, resulting in a significant correlation between E_{sat} and C_{fin} imposed by the mass filter. This explains the large posteriors obtained for the different NMP's with the $AME+R_{ch}$ and $Skin$ filters.

The correlations involving E_{sym} , L_{sym} and Q in the correlated sampling is a direct consequence of how they were populated following the correlation patch of Fig. 1. It is important to point out here that, we recover the correlation coefficient between Q and L_{sym} in the $AME+R_{ch}$ case (-0.79) as we started from Fig. 1 (-0.77). This clearly explains why a constraint on the skin impacts the properties of the symmetry energy, only if the surface stiffness parameter Q is *a-priori* well correlated to L_{sym} . If this is not the case, as assumed in the uncorrelated sample, the filters on the masses, charge radii and skin do not create such correlation, and the skin measurement is not constraining for the symmetry energy parameters.

The correlation plot for the $AME+R_{ch}$ filter alone is very similar to the case of $AME+R_{ch}+PREX-II+CREX$ filter. We display that explicitly in the supplemental material.

In Fig. 9 we display the correlation systematics obtained with the χ -EFT filter for the same set of observables as in Fig. 8. Quite recognizably, the correlation imposed *a-priori* between Q and L_{sym} in the correlated sample is reduced compared to the $AME+R_{ch}$ filter. Noticeable new correlations among pairs like $[E_{sat}-E_{sym}]$, $[n_{sat}-E_{sym}]$, $[E_{sym}-L_{sym}]$, $[L_{sym}-K_{sym}]$ appear unanimously for the two different sampling techniques of Q . Similar effect of χ -EFT filter on the empirical parameters were already observed in [38]. Considering that in a perfectly known EOS all the coefficients are strongly correlated by construction (even if the correlation does not need to be linear), this finding measures the amount of information on the behavior of the symmetry energy, brought in by the ab-initio calculations of nuclear mat-

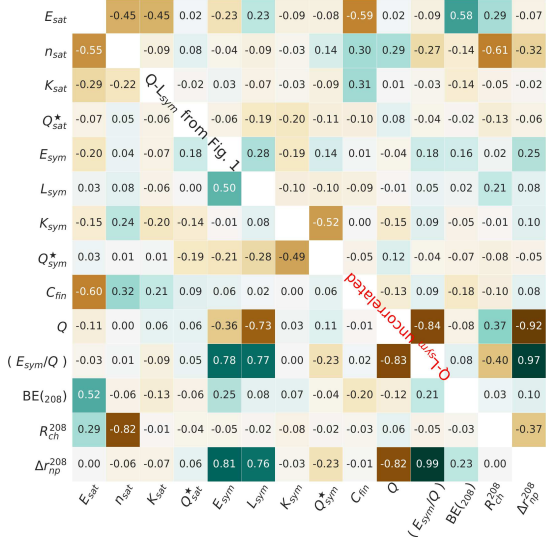


FIG. 10: (Color online) Same as Fig. 8, but obtained with *Astro* filter.

ter. In particular, the strong correlations $[K_{sat}-Q_{sat}]$ and $[K_{sym}-Q_{sym}]$ imply that, within a Taylor expansion truncated at some low order, the high density behavior of the EOS is strongly constrained in the χ -EFT posterior, even in a density region where the χ -EFT calculations cannot be safely extrapolated. This spurious behavior was discussed at length in Ref. [33]. In that paper, the authors showed that the low density behavior is spuriously extrapolated at densities higher than $\approx 0.4 \text{ fm}^{-3}$ even if the Taylor expansion is truncated at $N = 4$, meaning that the low and high density behavior of the EoS are effectively decoupled even in a purely nucleonic model. The impact of such spurious extrapolations was recently pointed out in ref.[79]. Conversely, it was shown in ref.[33] that this problem can be avoided if four extra parameters, describing the high density behavior and a-priori independent of the behavior at saturation, are called $Q_{sat,sym}^*$ and $Z_{sat,sym}^*$ in this paper.

Correlations obtained with the same set of observables as in Fig. 8-9 obtained with *Astro* filter is shown in Fig. 10. We can see that the correlations between the effective skewness parameters Q_{sat}^* , Q_{sym}^* and the low order parameters are very different from the ones of Fig. 9 associated to the skewness at and below saturation Q_{sat} , Q_{sym} , and well constrained by nuclear theory. The rest of the correlation plot is fairly similar to the one of Fig.8, except for the case between E_{sym} and E_{sym}/Q . It explains the prominent peaks observed for *Astro* posteriors of E_{sym}/Q and Δr_{np} 's in Fig. 7. But the overall strong resemblance with *AME+R_{ch}* case points to the fact that the low density physics is strongly decoupled from the high density one. Because of this, we expect a limited impact of the skin data on the astrophysical observables.

This above mentioned point is addressed in Figs. 11 and 12, where we display the tidal deformability Λ (left) and radii R (right) corresponding to $1.4M_{\odot}$ (up) and $2.0M_{\odot}$ (down) neutron stars, for the agnostic and correlated sampling of Q , respectively. As observed before in [38], the χ -EFT constraint

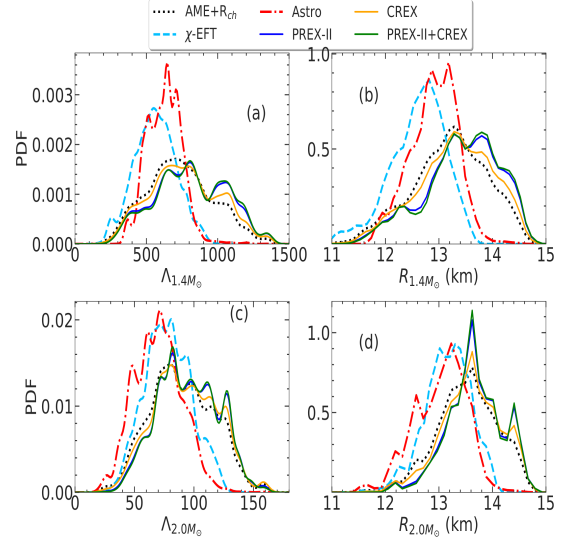


FIG. 11: (Color online) Posterior probability distribution of tidal deformability Λ (left panels) and radius R (right panels) corresponding to the $1.4M_{\odot}$ (top panels) and $2.0M_{\odot}$ (bottom panels) obtained with the models where surface stiffness Q is sampled independently from the bulk parameters in the prior.

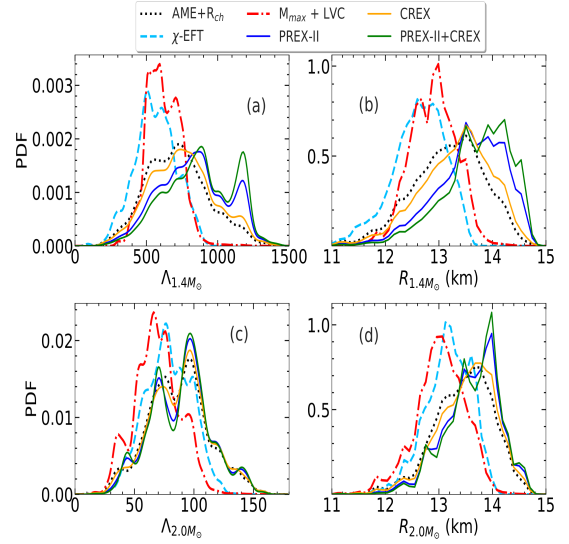


FIG. 12: (Color online) Same as Fig. 11 but with Q and L_{sym} correlated through Fig. 1.

produces posterior distributions of Λ and R that are perfectly compatible with the information that can be extracted from the astrophysical measurements through the *Astro* filter. This can be interpreted as a demonstration that nucleonic degrees of freedom can very well describe the present astrophysical information on neutron stars [38], and no evidence of deconfined matter can be inferred from the present data on radii and tidal deformability.

In all cases, χ -EFT and *Astro* filters cut off higher ends of the distributions of the experimental nuclear physics informed *AME+R_{ch}* distribution. Coming to the skin measurements, the

CREX filter shows absolute insensitivity to the concerned astrophysical observables, and the same is true to some extent for *PREX-II* as far as the very massive $2.0M_{\odot}$ neutron star is concerned. This can be easily understood from the already discussed effective decoupling between the low and high density domain that exists even in the conservative hypothesis of purely nucleonic degrees of freedom in the core of neutron stars, as shown in the correlation plots above. Concerning the $1.4M_{\odot}$ neutron star observables, however, we can observe some effect of the *PREX-II*, and hence *PREX-II+CREX* filters, shifting towards higher values the Λ and R distributions, particularly in the correlated sampling of Q . This directs towards an important impact of skin measurements on neutron-star observables [87], and a possible tension between low density and high density $M_{max}+LVC$ data that was interpreted as pointing towards the existence of a phase transition at high density [79, 88]. However, we observe that this tension already appears with respect to the χ -*EFT* filter that constrains the same density domain as *PREX-II+CREX*, and only appears if the surface parameter Q is robustly correlated with L_{sym} . Therefore, these findings do not support the interpretation of Ref. [88], and we rather associate this tension to the degree of interdependence between bulk and surface properties obtained by the underlying nuclear model. Deeper studies, probably beyond the mean-field picture, are needed to sort this problem out comprehensively [9, 11–13].

V. CONCLUSIONS

In this article, we present an upgradation of the nuclear metamodelling technique, to calculate the ground state properties of nuclei within the ETF method. This improvement allows combined and consistent Bayesian analyses of a plethora of theoretical and experimental data: not only the constraints from microscopic modelling can be treated consistently with the astrophysical observables within a unified treatment of the neutron star core and crust, but also nuclear data such as binding energies, charge radii and neutron skins can be addressed on the same footing, though within a simplified semiclassical approach. To this aim, two extra surface parameters are added to the parameter space of the bulk metamodelling, namely an isoscalar gradient coupling C_{fin} , and the surface stiffness parameter Q . Within any given homogeneous matter functional described through its associated NMP's, finite nuclei density profile are described with Fermi functions, with parameters

variationally obtained within a quasi-analytical version of the ETF theory.

In the present calculation, we particularly concentrated on the consequence of *CREX* and *PREX-II* results on our understanding of hadronic matter across wide range of densities covering both the subsaturation and the supersaturation regimes, in the hypothesis that an analytic behavior of the EoS is maintained up to the central densities of massive NSs. We addressed the issue of the connection between the recent skin data and the high density EoS, which is largely debated in the contemporary literature [8–10, 87], in a full Bayesian study with uncorrelated priors for the the high order and low order bulk parameters, and with different hypotheses on the correlations between bulk and surface.

Our main results can be summarized as follows. First, comparing the separate constraints coming from both *PREX-II* and *CREX*, we show that the skin value extracted from *PREX-II* is hardly compatible with the constraints coming from the requirement of reproducing nuclear masses over the whole mass range, in qualitative agreement with the conclusions of ref.[9]. We additionally demonstrate that a possible tension on the preferred values of L_{sym} extracted from the observation on tidal deformability from the LIGO-Virgo collaboration or the theoretical calculation of low density neutron matter using chiral effective field theory, and that from *PREX-II*, strongly depends on degrees of interdependence among bulk (slope L_{sym}) and surface (stiffness Q) parameters of the symmetry energy. To achieve the extremities of this interdependence, in one case, we sampled surface stiffness Q and L_{sym} independently and in the other, in a correlated manner, as suggested by several mean field models [76]. We conclude that the strong interplay between bulk and surface symmetry energy parameters is the primary reason behind the apparent tension between the preferred values of L_{sym} by *PREX-II* and other experiments or observations, while if this correlation is relaxed the tension disappears.

Finally, we critically discuss the impact of observables connected to ground state nuclear properties to astrophysical observables that are particularly sensitive to densities far beyond the nuclear saturation. We show that the subsaturation and supersaturation density domain are effectively decoupled even in the simplified nucleonic assumption. This implies that observations from nuclear physics and astrophysics are highly complementary for a full understanding of the nuclear equation of state.

-
- [1] S. Abrahamyan and et al., Phys. Rev. Lett. **108**, 112502 (2012).
 - [2] D. Adhikari and et. al (PREX Collaboration), Phys. Rev. Lett. **126**, 172502 (2021).
 - [3] D. Adhikari, H. Albatineh, D. Androic, K. A. Aniol, D. S. Armstrong, T. Averett, C. Ayerbe Gayoso, S. K. Barcus, V. Bellini, R. S. Beminiwatha, et al. (CREX Collaboration), Phys. Rev. Lett. **129**, 042501 (2022).
 - [4] A. Krasznahorkay, H. Akimune, A. van den Berg, N. Blasi, S. Brandenburg, M. Csatlós, M. Fujiwara, J. Gulyás, M. Harakeh, and M. H. et al., Nucl. Phys. **A731**, 224 (2004).
 - [5] B. Klos and et. al., Phys. Rev. C **76**, 014311 (2007).
 - [6] E. Friedman and et. al., Hyperfine Interact. **193**, 33 (2009).
 - [7] J. Zenihiro and et al., Phys. Rev. C **82**, 044611 (2010).
 - [8] P.-G. Reinhard, X. Roca-Maza, and W. Nazarewicz, Phys. Rev. Lett. **127**, 232501 (2021).
 - [9] P.-G. Reinhard, X. Roca-Maza, and W. Nazarewicz, arXiv:2206.03134v1 (2022).
 - [10] E. Yüksel and N. Paar, arXiv:2206.06527v1 (2022).

- [11] S. Typel, G. Röpke, T. Klähn, D. Blaschke, and H. H. Wolter, *Phys. Rev. C* **81**, 015803 (2010).
- [12] S. Typel, *Phys. Rev. C* **89**, 064321 (2014).
- [13] J. T. *et al.*, *Science* **371**, 260 (2021).
- [14] M. Centelles, X. Roca-Maza, X. Viñas, and M. Warda, *Phys. Rev. Lett.* **102**, 122502 (2009).
- [15] B. K. Agrawal, J. N. De, and S. K. Samaddar, *Phys. Rev. Lett.* **109**, 262501 (2012).
- [16] A. Pastore, *International Journal of Modern Physics E* **29**, 2050054-174 (2020).
- [17] C. Mondal, *Phys. Rev. C* **105**, 034305 (2022).
- [18] M. B. Tsang, T. X. Liu, L. Shi, P. Danielewicz, C. K. Gelbke, X. D. Liu, W. G. Lynch, W. P. Tan, G. Verde, A. Wagner, *et al.*, *Phys. Rev. Lett.* **92**, 062701 (2004).
- [19] P. Danielewicz, W. G. Lynch, and R. Lacey, *Science* **298**, 1592 (2002).
- [20] J. Adamczewski-Musch and *et al.* (HADES Collaboration), *Phys. Rev. Lett.* **125**, 262301 (2020).
- [21] P. Demorest, T. Pennucci, S. Ransom, M. Roberts, and J. Hessels, *Nature* **467**, 1081 (2010).
- [22] J. Antoniadis and *et al.*, *Science* **340**, 1233232 (2013).
- [23] T. E. Riley, A. L. Watts, S. Bogdanov, P. S. Ray, R. M. Ludlam, S. Guillot, Z. Arzoumanian, C. L. Baker, A. V. Bilous, D. Chakrabarty, *et al.*, **887**, L21 (2019).
- [24] M. C. Miller, F. K. Lamb, A. J. Dittmann, S. Bogdanov, Z. Arzoumanian, K. C. Gendreau, S. Guillot, A. K. Harding, W. C. G. Ho, J. M. Lattimer, *et al.*, **887**, L24 (2019).
- [25] T. E. Riley, A. L. Watts, P. S. Ray, S. Bogdanov, S. Guillot, S. M. Morsink, A. V. Bilous, Z. Arzoumanian, D. Choudhury, J. S. Deneva, *et al.*, **918**, L27 (2021).
- [26] M. C. Miller, F. K. Lamb, A. J. Dittmann, S. Bogdanov, Z. Arzoumanian, K. C. Gendreau, S. Guillot, W. C. G. Ho, J. M. Lattimer, M. Loewenstein, *et al.*, **918**, L28 (2021).
- [27] B. P. Abbott, R. Abbott, T. D. Abbott, F. Acernese, K. Ackley, C. Adams, T. Adams, P. Addesso, R. X. Adhikari, V. B. Adya, *et al.* (LIGO Scientific Collaboration and Virgo Collaboration), *Phys. Rev. Lett.* **119**, 161101 (2017).
- [28] B. P. Abbott, R. Abbott, T. D. Abbott, F. Acernese, K. Ackley, C. Adams, T. Adams, P. Addesso, R. X. Adhikari, V. B. Adya, *et al.* (The LIGO Scientific Collaboration and the Virgo Collaboration), *Phys. Rev. Lett.* **121**, 161101 (2018).
- [29] B. P. Abbott, R. Abbott, T. D. Abbott, F. Acernese, K. Ackley, C. Adams, T. Adams, P. Addesso, R. X. Adhikari, V. B. Adya, *et al.* (LIGO Scientific Collaboration and Virgo Collaboration), *Phys. Rev. X* **9**, 011001 (2019).
- [30] J. Aasi and *et al.*, *Classical and Quantum Gravity* **32**, 074001 (2015).
- [31] F. Acernese and *et al.*, *Classical and Quantum Gravity* **32**, 024001 (2014).
- [32] A. W. Steiner, J. M. Lattimer, and E. F. Brown, *Astrophys. J.* **765**, L5 (2013).
- [33] J. Margueron, R. Hoffmann Casali, and F. Gulminelli, *Phys. Rev. C* **97**, 025805 (2018).
- [34] N.-B. Zhang, B.-A. Li, and J. Xu, *Astrophys. J.* **859**, 90 (2018).
- [35] Y. Lim and J. W. Holt, *The European Physical Journal A* **55**, 11 (2019).
- [36] S. Traversi, P. Char, and G. Pagliara, *Astrophys. J.* **897**, 165 (2020).
- [37] B. Biswas, *Astrophys. J.* **921**, 63 (2021).
- [38] H. Dinh Thi, C. Mondal, and F. Gulminelli, *Universe* **7**, 373 (2021).
- [39] R. Essick, I. Tews, P. Landry, and A. Schwenk, *Phys. Rev. Lett.* **127**, 192701 (2021).
- [40] R. Somasundaram, I. Tews, and J. Margueron (2021), 2112.08157.
- [41] S. Ghosh, D. Chatterjee, and J. Schaffner-Bielich, *Eur. Phys. J. A* **58**, 37 (2022), 2107.09371.
- [42] S. M. A. Imam, N. K. Patra, C. Mondal, T. Malik, and B. K. Agrawal, *Phys. Rev. C* **105**, 015806 (2022), 2110.15776.
- [43] C. Mondal and F. Gulminelli, *Phys. Rev. D* **105**, 083016 (2022).
- [44] T. Malik, M. Ferreira, B. K. Agrawal, and C. Providência, *Astrophys. J.* **930**, 17 (2022), 2201.12552.
- [45] S. H. Völkel and C. J. Krüger, *Phys. Rev. D* **105**, 124071 (2022).
- [46] S. Huth, P. Pang, I. Tews, T. Dietrich, A. Le Fèvre, A. Schwenk, W. Trautmann, K. Agarwal, M. Bulla, M. Coughlin, *et al.*, *Nature* **606**, 276 (2022).
- [47] X. Roca-Maza and N. Paar, *Prog. Part. Nucl. Phys.* **101**, 96 (2018).
- [48] J. D. Walecka, *The Relativistic Nuclear Many-Body Problem* (Springer US, Boston, MA, 1986), pp. 229–271, ISBN 978-1-4684-5179-5.
- [49] T. H. R. Skyrme, *Phil. Mag.* **1**, 1043 (1956).
- [50] T. H. R. Skyrme, *Nucl. Phys.* **9**, 615 (1959).
- [51] J. Decharge and D. Gogny, *Phys. Rev. C* **21**, 1568 (1980).
- [52] W. Ryssens and M. Bender, *Phys. Rev. C* **104**, 044308 (2021).
- [53] J. Xu and P. Papakonstantinou, *Phys. Rev. C* **105**, 044305 (2022).
- [54] F. Aymard, F. Gulminelli, and J. Margueron, *J. Phys. G* **43**, 045105 (2016).
- [55] F. Aymard, F. Gulminelli, and J. Margueron, *J. Phys. G* **43**, 045106 (2016).
- [56] D. Chatterjee, F. Gulminelli, A. R. Raduta, and J. Margueron, *Phys. Rev. C* **96**, 065805 (2017).
- [57] H. D. Thi, T. Carreau, A. F. Fantina, and F. Gulminelli, *Astron. Astrophys.* **654**, A114 (2021).
- [58] H. Dinh Thi, A. F. Fantina, and F. Gulminelli, *Eur. Phys. J. A* **57**, 296 (2021).
- [59] L. Suleiman, M. Fortin, J. L. Zdunik, and P. Haensel, *Phys. Rev. C* **104**, 015801 (2021), 2106.12845.
- [60] S. Typel *et al.* (2022), 2203.03209.
- [61] M. Dutra, O. Lourenço, J. S. Sá Martins, A. Delfino, J. R. Stone, and P. D. Stevenson, *Phys. Rev. C* **85**, 035201 (2012).
- [62] M. Dutra, O. Lourenço, S. S. Avancini, B. V. Carlson, A. Delfino, D. P. Menezes, C. Providência, S. Typel, and J. R. Stone, *Phys. Rev. C* **90**, 055203 (2014).
- [63] X.-H. Li, W.-J. Guo, B.-A. Li, L.-W. Chen, F. J. Fattoyev, and W. G. Newton, *Phys. Lett. B* **743**, 408 (2015).
- [64] Z. Zhang and L.-W. Chen, *Phys. Rev. C* **93**, 034335 (2016).
- [65] H.-Y. Kong, J. Xu, L.-W. Chen, B.-A. Li, and Y.-G. Ma, *Phys. Rev. C* **95**, 034324 (2017).
- [66] C. Mondal, B. K. Agrawal, J. N. De, and S. K. Samaddar, *International Journal of Modern Physics E* **27**, 1850078 (2018).
- [67] C. Mondal, Ph.D. thesis, HBNI, Mumbai (2017), 1808.07473.
- [68] T. Carreau, F. Gulminelli, and J. Margueron, *Eur. Phys. J. A* **55**, 188 (2019), 1902.07032.
- [69] D. G. Ravenhall, C. J. Pethick, and J. M. Lattimer, *Nucl. Phys. A* **407**, 571 (1983).
- [70] M. Wang, G. Audi, F. G. Kondev, W. Huang, S. Naimi, and X. Xu, *Chinese Physics C* **41**, 030003 (2017).
- [71] U. a. J. Furtado and F. Gulminelli, *J. Phys. G* **48**, 015102 (2020), 2010.01227.
- [72] G. Grams, J. Margueron, R. Somasundaram, N. Chamel, and S. Goriely (2022), 2205.15091.
- [73] T. Carreau, F. Gulminelli, N. Chamel, A. F. Fantina, and J. M. Pearson, *Astron. Astrophys.* **635**, A84 (2020), 1912.01265.
- [74] G. Scamps, S. Goriely, E. Olsen, M. Bender, and W. Ryssens, *European Physical Journal A* **57**, 333 (2021).
- [75] A. Bhagwat, M. Centelles, X. Viñas, and P. Schuck, *Phys. Rev.*

- C **103**, 024321 (2021).
- [76] M. Warda, X. Viñas, X. Roca-Maza, and M. Centelles, Phys. Rev. C **80**, 024316 (2009).
- [77] F. Buchinger, J. E. Crawford, A. K. Dutta, J. M. Pearson, and F. Tondeur, Phys. Rev. C **49**, 1402 (1994).
- [78] Z. Patyk, A. Baran, J. F. Berger, J. Dechargé, J. Dobaczewski, P. Ring, and A. Sobiczewski, Phys. Rev. C **59**, 704 (1999).
- [79] B. Biswas, P. Char, R. Nandi, and S. Bose, Phys. Rev. D **103**, 103015 (2021).
- [80] M. Farine, J. Côté, and J. M. Pearson, Phys. Rev. C **24**, 303 (1981).
- [81] I. Angeli and K. Marinova, Atomic Data and Nuclear Data Tables **99**, 69 (2013).
- [82] C. Drischler, K. Hebeler, and A. Schwenk, Phys. Rev. C **93**, 054314 (2016).
- [83] P. Klüpfel, P.-G. Reinhard, T. J. Burvenich, and J. A. Maruhn, Phys. Rev. C **79**, 034310 (2009).
- [84] C. Mondal, B. K. Agrawal, J. N. De, and S. K. Samaddar, Phys. Rev. C **93**, 044328 (2016).
- [85] K. Washiyama, K. Bennaceur, B. Avez, M. Bender, P.-H. Heenen, and V. Hellemans, Phys. Rev. C **86**, 054309 (2012).
- [86] M. Bender, G. F. Bertsch, and P.-H. Heenen, Phys. Rev. C **73**, 034322 (2006).
- [87] B. T. Reed, F. J. Fattoyev, C. J. Horowitz, and J. Piekarewicz, Phys. Rev. Lett. **126**, 172503 (2021).
- [88] H. Güven, K. Bozkurt, E. Khan, and J. Margueron, Phys. Rev. C **102**, 015805 (2020).